Dryline characteristics in North America's historical and future climates

Lucia Scaff[1*], Andreas F. Prein[2], Yanping Li[1], Adam J. Clark[3], Sebastian A. Krogh[4,5], Neil Taylor[6], Changhai Liu[2], Roy M. Rasmussen[2], Kyoko Ikeda[2], Zhenhua Li[1].

1. Global Institute for Water Security, University of Saskatchewan. 11 Innovation Blvd, Saskatoon, SK S7N 3H5, Canada
2. NCAR National Center for Atmospheric Research. 3090 Center Green Drive, Boulder, CO 80301, USA
3. NOAA/OAR/National Severe Storms Laboratory, National Weather Center, Norman, OK 73072, USA
4. Departamento de Recursos Hídricos, Facultad de Ingeniería Agrícola, Universidad de Concepción, Chillán, 3812120, Chile
5. Department of Natural Resources and Environmental Science, University of Nevada, Reno, NV 89557, USA
6. Applied Environmental Prediction Science - Prairie and Northern, Meteorological Service of Canada (MSC), Environment and Climate Change Canada, Edmonton, AB, T6B 1K5

* Corresponding Author. Contact: lucia.scaff@usask.ca, https://orcid.org/0000-0002-6481-2652

Abstract

Drylines are atmospheric boundaries separating dry from moist air that can initiate convection. Potential changes in the location, frequency, and characteristics of drylines in future climates are unknown. This study applies a multi-parametric algorithm to objectively identify and characterize the dryline in North America using convection-permitting regional climate model simulations with 4-km horizontal grid spacing for 13-years under a historical and a pseudo-global warming climate projection by the end of the century.

The dryline identification is successfully achieved with a set of standardized algorithm parameters across the lee side of the Rocky Mountains from the Canadian Rockies to the Sierra Madres in Mexico. The dryline is present 27% of the days at 00 UTC between April and September in the current climate, with a mean humidity gradient magnitude of 0.16 g^{-1} kg^{-1} km^{-1}. The seasonal cycle of drylines peak around April and May in the southern Plains, and in June and July in the northern Plains. In the future climate, the magnitude and frequency of drylines increase 5% and 13%, correspondingly, with a stronger intensification southward. Future drylines strengthen during their peak intensity in the afternoon in the Southern U.S. and Northeast Mexico. Drylines also show increasing intensities in the morning with future magnitudes that are comparable to peak intensities found in the afternoon in the historical climate. Furthermore, an extension of the seasonality of intense drylines could produce end-of-summer drylines that are as strong as mid-summer drylines in the current climate. This might affect the seasonality and the diurnal cycle of convective activity in future climates, challenging weather forecasting and agricultural planning.

Key words

- Dryline
- Convection-permitting modeling
- Pseudo Global Warming
- Rocky Mountains

Declarations

Funding (information that explains whether and by whom the research was supported)

This research was supported by the Tri-agency Institutional Programs Secretariat of Canada through the Global Water Futures Program, Canada First Research Excellence Fund.

Conflicts of interest/Competing interests (include appropriate disclosures)

On behalf of all authors, the corresponding author declare no conflict of interest and no competing interests.

Availability of data and material (data transparency)

The CONUS simulations are available in the dataset DS612.0 at the Research Data Archive operated by the Computational and information System Lab at the National Center for Atmospheric Research.

Code availability (software application or custom code)

The data processing was built using NCL, MATLAB and Python. The scripts can be available upon request to the corresponding author.

Authors' contributions

LS designed the study, and process and analyzed the data. LS, AP, AC and SK contributed to guiding the results and discussion. KI and CL performed the CONUS simulations. All coauthors contributed to writing the manuscript.

1 Introduction

Convective thunderstorms can generate severe weather (Rhea 1966) with significant impacts on the population, representing a great prediction challenge for weather forecasters (Fritsch and Carbone 2004). Convective precipitation can be triggered by atmospheric boundaries (Wilson and Schreiber 1986) such as the dryline. The dryline is a near-surface horizontal moisture boundary between a dry-hot and a moist-warm air-mass (Schaefer 1974), which is intensified by the diurnal variation of the boundary layer (Sun and Wu 1992). The dryline can induce severe convection in environments with high wind shear and buoyancy (Ziegler and Rasmussen 1998); however, forecasting such storms is challenging partially due to uncertainties in the triggering potential of the dryline. Drylines typically form at the lee side of mountainous regions, with similar characteristics in different regions of the World, such as the North American Great Plains (Rhea 1966, Parsons et al. 1990, Taylor et al. 2011), Central Argentina (Bechis et al. 2020), Northwest Australia (Arnup and Reeder 2007), and Northern India (Weston 1972).

The dryline in North America is generated by a confluence of the low-level jet transporting moisture from the Gulf of Mexico to the Central Plains east of the Rocky Mountains, along with the subsidence of dry westerly flow (Schaefer 1974). The terrain gradient across the Great Plains also plays a crucial role in the development of the dryline. The dryline marks the intersection between the top of the moist boundary layer originating from the Gulf of the Mexico with the gently rising terrain from east to west across the Central Plains. The dryline is an elongated feature commonly defined by a strong moisture gradient rather than a thermal gradient. For example, Hoch and Markowski (2005) defined the dryline using a water vapor mixing ratio gradient greater or equal than 0.03 g kg^{-1} km^{-1} in the southern U.S. Their definition has been used to identify drylines in different regions (Coffer et al. 2013; Bergmaier and Geerts 2015; Duell and Van Den Broeke 2016; Bechis et al. 2020) allowing for a comparison between studies and across regions. The humidity gradient produces an imbalance in the atmosphere, which is then compensated by a solenoidal circulation (increased solenoidal term in the vorticity equation) that interacts with the convergence flow at low levels close to the strongest humidity gradient (Ziegler et al. 1997). Thus, the convergence zone along with the solenoidal circulation lifts air parcels (Ziegler et al. 1997) that can result in convective initiation (CI) in its vicinity (Rhea 1966; Ziegler and Rasmussen 1998).

Drylines have been observed on 32% of days between April and June over the Great Plains (30 years of analysis, Hoch and Markowski 2005), whereas in southwest Wyoming around 11% of days between April and June show a dryline with an average gradient of 5.3 g kg^{-1} 100 km^{-1} (using three years of Reanalysis data; Bergmaier and Geerts 2015). Drylines with different widths have been observed and simulated ranging from less than 1-km (e.g. Ziegler and Rasmussen 1998; Sipprell and Geerts 2007) to 3-9 km wide (e.g. Ziegler et al. 1997; Peckham et al. 2004; Xue and Martin 2006). Maximum across-dryline water vapor mixing ratio differences spanning dryline widths of up to 5 g/kg over 2 km (Ziegler and Hane, MWR, 1993; Ziegler and Rasmussen ,1998), 3 g/kg over 3 km (Hane et al., MWR, 1997), 4 g/kg over 1.5 km (Buban et al., 2007), 2 g/kg over 2 km (Ziegler et al., MWR, 2007), and 1.3 g/kg over 0.15 km (Sipprell and Geerts, 2007) have also been observed in situ by mobile surface and airborne platforms at fine spatial scales on the U.S. plains.

Drylines are mostly associated within the meso-gamma scale between 2 and 20 km (Miao and Geerts 2007), showing an spatial complexity that challenges an accurate and automatic detection (Buban et al. 2007). In other regions, such as the Canadian Rockies, field campaigns (Strong 1989; Hill 2006; Taylor et al. 2011) and high-resolution atmospheric models (Erfani et al. 2003; Taylor et al. 2011) have been used to investigate drylines. For example, a dryline with a humidity zonal gradient between 0.9 and 4.3 g kg^{-1} km^{-1} was found during the initiation of rainfall (Hill, 2006). And more recently, Taylor et al. (2011) found a dryline with a humidity gradient of up to 18 g kg^{-1} km^{-1} in their latest field experiment.

These and other case studies have improved our understanding of the dryline dynamics and its effect on convective precipitation; however, the detection of drylines has been somewhat subjective and varies between researchers and regions. This is partially due to the fact that they only consider thermodynamic thresholds of moisture and temperature, and wind circulation, whereas information about dryline geometry and temporal features are implicitly evaluated by the forecaster. This subjectivity becomes an issue for cross-regional intercomparison studies, thus the need to develop an automatic algorithm that can detect drylines at regional and multi-temporal scales. Previous studies have developed objective and automatic algorithms to detect drylines (Clark et al. 2015b; Duell and Van Den Broeke 2016; Bechis et al. 2020) in different regions; however, no study has provided a definition that reliably detects drylines across regions, and then applied it over many years (>10 years). Moreover, the potential impact of climate change on the dryline regional characteristics has not been investigated. Historically, automatic detection algorithms have been challenged by our limited computational capabilities and ability to simulate mesoscale processes over climate time scales, and the relatively coarse spatial density of surface moisture gradient observations to validate simulations. Automatic algorithms can also be used to identify how a warmer climate might alter dryline characteristics and other processes such as changes in soil moisture (Flanagan et al. 2017; Johnson and Hitchens 2018), highlighting the need for more research in this direction.

The purpose of this study is to characterize the dryline at the lee side of the Rocky Mountains in a historical and a warmer climate simulation based on a modified version of the automatic algorithm presented by Clark et al (2015). We aim to answer the following questions: (1) Can we develop objective and automated criteria to consistently identify drylines across a regional domain? (2) How does the frequency, duration and magnitude of drylines vary temporally and spatially over North America? And (3) how might this change under a warmer climate?

2 Datasets

The Weather Research and Forecasting model (WRF, Skamarock et al. 2008; Powers et al. 2017) version 3.4.1. was used to simulate the historical climate (CTRL) from 2001 to 2013 in North America (Liu et al., 2017). CTRL simulation was forced with the ERA-Interim reanalysis (Dee et al. 2011) as the boundary and initial conditions. A Pseudo Global Warming approach (PGW, Schär et al. 1996; Rasmussen et al. 2011) was used to simulate future climate under the RCP8.5 scenario by the end of the century. Both simulations were performed over the same continental domain (Fig. 1) at a horizontal grid spacing of 4 km in a convection-permitting configuration (i.e. no deep convection scheme was applied), and used spectral nudging of state variables (except air moisture) above the planetary boundary layer on scales larger than 2,000 km. More details about the model configuration and documentation of the experimental design and quality are presented in Table 1 and in Liu et al. (2017).

It is generally recognized that the shortest resolved scales in WRF are about six times the grid spacing (e.g., Skamarock, 2004). However, the longest wavelength at which the model cannot detect wavelike humidity gradients is the Nyquist wavelength, which is twice the grid spacing. Approximating a dryline gradient zone as a half-sinusoid, drylines wider than 12 km (i.e., 3 x delta-x) can be approximately resolved, while narrower drylines are expected to be more poorly resolved. Thus, the simulations are at least partially resolving drylines at wavelengths between 8 and 24 km, and completely resolving the dryline at wavelengths greater than 24 km. This means that the shortest wavelengths of very sharp drylines may not always be adequately resolved by the model, but this does not pose a significant issue for this study in a climatological scale, because the algorithm will identify some of these sharp drylines based on the larger component wavelengths that are resolved.

The future PGW simulations were created by perturbing ERA-Interim reanalysis lateral boundary and initial conditions with a climate change delta. These perturbations were based on 100-year, monthly-mean climate change signals of several state variables (air temperature, humidity, wind speed, geopotential heights, and sea surface temperatures) from an ensemble of 19 global climate models from the Coupled Model Intercomparison Project Phase 5 (CMIP5; Taylor et al 2012) under a high-emission scenario (RCP8.5, Riahi et al 2011). Historical simulations have been validated, and used along with future simulations for regional studies, such as the verification of the precipitation diurnal cycle in summer and changes in a warmer climate (Scaff et al. 2019), future intensification of precipitation extremes (Prein et al. 2016), simulation and changes in mesoscale convective systems (Prein et al. 2017a, b), future changes in the thermodynamics of deep convection (Rasmussen et al. 2017), and changes in hurricanes (Gutmann et al. 2018).

The ERA5 reanalysis (ECMWF 2017) is selected to compare the monthly average of water vapor mixing ratio at 2 m above the surface against the CTRL simulation. ERA5 is chosen because of its higher spatial (~0.28°) and temporal resolution (hourly) compared with other reanalyses (e.g., Dee et al. 2011; Saha et al. 2010).

3 Method

3.1 Study domain

The dryline is analyzed over the leeside of the Rocky Mountains, which we divide into four subdomains from north to south (Fig. 1). The four subdomains overlap by about three degrees of latitude and are selected based on previous studies in these regions (e.g. Taylor et al. 2011; Campbell et al. 2013; Clark et al. 2015). The northern subdomain covers the Canadian Rocky Mountains in the Province of Alberta (similar to Taylor et al. 2011), the second subdomain covers the northern part of the U.S. Rockies (NUS, similar to Campbell et al. 2013), the third domain includes from southern Wyoming to northern Texas (SUS) (similar to Coffer et al. (2013) and Clark et al. (2015)), and the fourth domain includes from southern Texas to northern Mexico (NMX) excluding the coast.

3.2 Numerical model validation

The CTRL simulation is verified against the ERA5 reanalysis (Hersbach et al. 2020) for the period 2001-2013. The average water vapor mixing ratio at 2 m is calculated from May to August using dewpoint temperature at 2 m and surface pressure. ERA5 is re-gridded to 4 km using a bilinear interpolation approach to match the CTRL simulation grid. This bilinear interpolation is from the Earth System Modeling Framework (ESMF) toolbox included in NCAR Command Language (NCL). As ERA5 has been shown to be a superior product (Hersbach et al. 2020) we chose to use it for validation instead of ERA-Interim.

3.3 Drylines automatic identification

The multiparametric algorithm presented by Clark et al. (2015) and documented by MacKenzie (2013) is adjusted to objectively and automatically identify drylines in all four subdomains. The original method is divided into three steps. First, it calculates moisture gradients using a smoothing Gaussian filter and applies a cutoff to the gradients of water vapor mixing ratio, dewpoint temperature and water vapor pressure at 2 m above the surface. These gradients are calculated using a 3x3 Sobel operator (Weeks 1996) for edge detection in image processing. Second, an independent smoothing and binary dilation over humidity is processed using a non-maximum suppression algorithm (Sun and Vallotton 2009) to find unique and continuous lines of maximum gradients. One limitation of this step is the simplification of one dryline in a neighbouring region, which can miss secondary/minor parallel drylines. Third, the result of the previous two steps are combined using masks and binary logical operators to select the most probable dryline. The third step uses gradient thresholds and criteria for a minimum width and length of the bounding box containing the dryline.

The magnitude of the water vapor mixing ratio gradient is calculated using the square root of the sum of the squared latitudinal gradient and the squared zonal gradient, considering positive zonal gradients only (dry air at the west and moist air at the east). A dryline must have a water vapor mixing ratio gradient ≥ 0.03 g kg^{-1}km^{-1} (Hoch and Markowski 2005; Coffer et al. 2013), and a dewpoint temperature gradient ≥ 0.055 K km^{-1} (Clark et al. 2015). We perform a sensitivity analysis to define the most effective combinations of vapor pressure gradients and geometric characteristics thresholds (minimum bounding box size) to identify drylines across the four subdomains. This analysis aims to detect documented cases in SUS, which is the only subdomain containing a dataset of manually detected drylines for several years (131 events,

Table 2; from Geerts et al. 2006; Coffer et al. 2013 and Clark et al. 2015) between 2007 and 2012 from April to June at 00 UTC. The threshold values presented by Clark et al. (2015) are used as a starting point to find a set of standard parameters for all subdomains. The sensitivity of the algorithm in SUS is presented in a performance diagram (Roebber 2009).

3.4 Characterization of the dryline

The dryline is characterized by its magnitude, frequency, location, diurnal and seasonal cycle, and its major axis distance, using the original model output (without smoothing). The mean monthly magnitude of the dryline is calculated as the average of all the events in each month between April and September over the 13-year period at 00 UTC for consistency with previous studies (Hoch and Markowski 2005; Coffer et al. 2013; Bergmaier and Geerts 2015). The diurnal cycle of the dryline is calculated as the average of its magnitude for each hour and month. Several geometrical features of the dryline's spatial extent are examined using an image processing toolbox (Mathworks 2014); however, we focus on the length of the major dryline axis as it presents an interesting seasonal cycle variation. These characteristics are examined under the CTRL and PGW scenarios, and the non-parametric Mann-Whitney rank sum test is performed to quantify the differences at a significant level of 5% (Wilks 2011, p. 159).

4 Results

4.1 Model Verification

A comparison between the ERA5 reanalysis and CTRL simulation (2001-2013 period) of the low-level water vapor mixing ratio is presented from May to August (Figure 2). Both datasets have a similar continental spatial pattern, with comparable magnitudes over the dry and moist side of the longitudinal gradient, ranging from 4-7 g kg^{-1} over the Rockies to 10-15 g kg^{-1} in the

Great Plains. However, during July and August the CTRL simulation shows a less extended continental moist air mass from the Gulf of Mexico to the Midwest compared to the ERA5, which reaches far northward into the northern Great Plains. This is consistent with a general warm and dry bias in the CTRL simulation over the Central U.S. during summer months (Liu et al. 2017). A persistent dry bias is present in the west coast through all months, that is around 60% drier in the CTRL than in the ERA5 over California. We expect that these biases will not greatly affect the characterization of the dryline in the four subdomains.

4.2 Parameters sensitivity analysis

The automatic detection algorithm is sensitive to the vapor pressure gradient threshold across the subdomains; however, it is less sensitive when a restrictive threshold for the dryline bounding box length is set (Figure 3). After 19 parameter combinations (Table 3), we find that removing the vapor pressure gradient (i.e. threshold = 0 hPa) and imposing a bounding box length ≥ 600 km, results in the best performance in SUS (Figure 3). Of the 131 documented drylines between 2007 and 2012 (Table 2, Geerts et al. 2006, Coffer et al. 2013 and Clark et al. 2015), 119 are found in the CTRL simulation; however, the algorithm identifies another 195 cases. This results in a probability of detection of 91% (correctly simulated cases over the total observed cases) and a success ratio of 38%, which is 1 minus false alarm ratio (FAR is the wrongly simulated cases over the total simulated cases, ~62%). The bounding box criteria removes atmospheric boundaries with a strong moisture gradient that are not typically considered as drylines, such as frontal lines and storms outflows (Coffer et al. 2013); however, it can also exclude short drylines (with a bouding box length <600 km). On the other hand, the over-identification of drylines is partially explained by cases that might not be documented and by systematic issues of overdetection by the algorithm when no additional tools such as machine learning is applied (Clark et al., 2015). The best results with the sensitivity analysis are thresholds of: water vapor mixing ratio gradient ≥ 0.03 g kg^{-1} km^{-1}, dewpoint temperautre gradient ≥ 0.055 K km^{-1}, and drylines contained in a bounding box of at least 600 km long and 220 km wide. These criteria minimize the chance of false-positve detection (Figure 3), and are then used to detect drylines across the four subdomains during historical and warmer climate.

An example of an automatically identified dryline is shown in Figure 4 (see the supplementary material for more examples). On 07 June of 2007 at 00 UTC, the dryline is correctly detected along the Rockies in the SUS subdomain (green contours, Figure 4, upper right panel), as also manually detected by Coffer et al. (2013) (Figure 4, lower right panel). Both the observed and automatically detected dryline show a similar location and orientation; however, the automatically detected dryline is slightly longer than observed spanning from the west of Texas to the south of South Dakota. It is important to note that the dataset used to identify the dryline are different, as Coffer et al, 2013 used RUC analysis while the CONUS I simulation from WRF is used in this study. The automatically detected dryline shows an average and maximum water vapor mixing ratio gradient of 0.23 and 0.59 g kg^{-1} km^{-1}, correspondingly, and its major axis length is around 363 km. The future simulation also shows that the automatic detection algorithm identifies a strong north-south oriented dryline, slightly shorter in the northernmost end (Figure 4). However, other examples such as in Figure S2, shows as extension of the dryline to the north in the future simulation. The average and maximum humidity gradient is 0.24 and 0.57 g kg^{-1} km^{-1}, correspondingly, and its major axis length is around 333 km.

4.3 Regional Dryline characteristics

The dryline's average daily frequency at 00 UTC between April and September is 27% (49 days) (Table 4) in the CTRL simulation (Figure 5). At the subdomain scale, the frequency varies from 9% (17 days) in CR to 47% (86 days) in SUS. Across all subdomains, the frequency increases in the future (Table 4). On average, the mean frequency increases to 31% (4% increase), ranging from 16% (29 days) in CR to 51% (93 days) in SUS. This change is statistically significant in some months across the subdomains (see grey regions in Figure 6). For example, the frequency increase is significant in May, June, August and September in the CR, but only in April for NMX.

The average number of drylines per grid cell shows a similar spatial pattern in the CTRL and PGW simulations, with an increase number of events in the future (Figure 5, upper panels). The most recurrent location in CR is constrained to the east of the foothills, between 54°N -50°N and 118°W-113°W. This subdomain also shows the largest increase in the number of dryline events over the entire domain (7%, Table 4), with values up to 29 days in the future. In the Central U.S., drylines are more frequent and spread over the central Great Plains, between 105°W and 95°W, with an intensification south of 42°N. The frequency in NMX is strong and it is confined in the east by the Sierra Madre Oriental. The dryline's maximum magnitude per grid cell (Figure 5, lower panels) shows the highest values in the SUS, with values up to 1.28 g^{-1} kg^{-1} km^{-1} that decline to the north, whereas CR shows a maximum of 0.69 g^{-1} kg^{-1} km^{-1}. CR has the largest increase in maximum magnitude for the future, with values up to 1.05 g^{-1} kg^{-1} km^{-1} (52% increase, not shown).

When we look at the subdomains from north to south, the seasonality of the dryline magnitude and frequency shows an earlier maximum in the future (Figure 6). Magnitude peaks earliest in April/May in NMX and SUS, June in NUS, and July in CR. The monthly average dryline magnitude in the CTRL ranges from 0.11 to 0.15 g kg^{-1} km^{-1} in CR and from 0.16 to 0.23 g kg^{-1} km^{-1} in NMX. The magnitude intensifies in the PGW across all subdomains. The dryline magnitude shows a statistically significant increase in the PGW (grey areas in Figure 6) from July to September in CR, and in April, June and July for NUS, most months in SUS and from April to July in NMX.

The dryline major axis length (right panels, Figure 6) shows no overall change in the PGW compared to the CTRL (0%, Table 4). The only significant change occurs in NUS during August decreasing 16% or 76 km. There is a distinct seasonal pattern in the dryline length between the northern (CR and NUS) and southern (SUS and NMX) subdomains (Figure 6). CR shows maximum length values in midsummer (June and July) with little seasonality, whereas the southern subdomain (SUS and NMX) has its maximum earlier in the summer (May). This is possibly linked to the North American Monsoon circulation, which decreases the moisture gradient in the southern part of the domain, normally beginning in June (Hoch and Markowski 2005).

We analyze the mean monthly diurnal cycle of the dryline in all subdomains and summer months (Supplementary Figures S10-S17); however, we focus on months when the magnitude of the dryline is the largest (Figure 6). The northern subdomains (CR and NUS) have their maximum magnitude in June and July (Figure 7), and their diurnal cycle fluctuates from 0.1 to 0.19 g kg^{-1} km^{-1}. The southern subdomains (SUS and NMX) have their maximum mean monthly dryline's magnitude in April and May, and the diurnal cycle ranges from 0.14 to 0.3 g kg^{-1} km^{-1} (Figure 8).

The maximum magnitude of the dryline occurs around 21-24 h in local time throughout the domain (Mountain Daylight Time, MDT), which is 03-06 UTC. The minimum value occurs around 06 and 12 h MDT in CR and NUS (around 12-18 UTC), while in the southern subdomains it takes place at 12-17 h MDT (around 18-23 UTC). During the hours of maximum magnitude, the PGW shows an intensification in most hours. Furthermore, in the PGW and over NMX, SUS and NUS, the morning dryline magnitudes are comparable with the afternoon magnitude in the current climate.

5 Discussion

The dryline is a frequent feature at the lee side of the Rocky Mountains and has been studied by the forecasting community because of its impact on convective initiation (Rhea 1966). This study shows the difficulties to objectively and automatically identify the dryline in a continental domain, exposing the need to unify the dryline definition. We propose a calibrated multi-parametric algorithm that shows promising potential to enable such unification. We apply the multi-parametric algorithm over a historical convection-permitting simulation that successfully captured the main continental patterns of the humidity seasonal variation, which is critical for the dryline detection. The water vapor mixing ratio seasonal development at low levels coincides with a strong decrease of the dryline magnitude after June in SUS and NMX. This has been associated with the increasing moisture fluxes to the dry side (west) of the dryline associated with the North American Monsson decreasing the moisture gradient (Hoch and

Markowski 2005). Challenges in representing humidity in the central Plains are found (Figure 2), consistent with previous studies (Coffer et al. 2013; Coniglio et al. 2013).

The dryline width was explored as a proxy to evaluate the limitation of representing the dryline in a simulation at 4 km grid spacing. Drylines in such a simulation will approximately resolve half-sinusoidal wavelike gradients, which are wider than 12 km (3Δx) but will not resolve wavelike gradients smaller or equal to 4 km in width (corresponding to half the Nyquist wavelength). The drylines in this study are on average around 15 km wide (see Fig. S9) and below 19 km, which keeps the automatically detected drylines out of the meso-beta scale (20-200 km). Therefore, the CTRL simulation is only representing the upper end of the observed drylines, which is within the longwave end of the meso-gamma scale (2 km - 20 km). For this reason, we compare our results with studies that use datasets with grid-spacing 4 km or larger.

Historically, the most studied region for drylines has been the SUS (e.g. Rhea 1966; Hane et al. 1993; Trier et al. 2004; Wilson and Roberts 2006; Clark et al. 2015a), where we find the highest dryline frequencies. For example, we show that between April and June, 55% of the days have a dryline at 00 UTC in SUS, as opposed to 32% by Hoch and Markowski (2005), or 34% days between 2006 and 2015 in Oklahoma (Johnson and Hitchens 2018). Other studies have found higher dryline frequency of around 41-45% (Rhea 1966; Schaefer 1973; Peterson 1983) between April and June for different years. However, this study shows the highest frequency percentage in SUS. This characteristic is consistent with the systematic overprediction by the multi-parametric algorithm, as mentioned before in this study and in Clark et al., 2013.

In NUS, the dryline frequency is 33% (between May and August), which is also higher than previous findings in Wyoming of 11% of the days (Bergmaier and Geerts 2015) for three years (2010-2012). This could be partly due to the use of a coarse-resolution gridded reanalysis data at 32-km resolution in Bergmaier and Geerts (2015). In NUS, the dryline average magnitude is 0.15 g kg^{-1} km^{-1}, which is similar to previous studies in Wyoming with values between 0.05 to 0.1 g kg^{-1} km^{-1} (Bergmaier and Geerts, 2015). Meanwhile in CR, we find that the magnitude of the dryline (0.13 g kg^{-1} km^{-1}) is lower than previously observed in the Canadian Rockies (0.9 to 4.3 g kg^{-1} km^{-1} in Hill (2006)).

Different frequencies and magnitudes are not only associated with the region and the horizontal grid spacing of the datasets, but also with the source of data (e.g. observed vs simulated) and the methodology employed to estimate the humidity gradient. For example, the manual identification of drylines is potentially more time-consuming, requires highly trained staff and is prone to the personnel's subjective criteria. In contrast, the automatic detection algorithm is replicable, and potentially transferrable across regions, but it is subject to the selection of parameters thresholds regarding thermodynamic and geometric features that may be hard to define.

We tested the sensitivity of the algorithm to such decisions against a series of documented dryline cases in the Great Plains (Table 2). This analysis revealed that thresholds regarding the geometric characterization of the dryline (width and length of the bounding box containing the dryline) help with the removal of atmospheric boundaries associated with cold pools and precipitation. These features are normally shorter than typical drylines as defined in the literature (Coffer et al., 2013). However, to fully explores the sensitivity of this method to parameter thresholds, more parameter combinations are needed, which is challenging due to the significant computational resources that are required. For instance, the geometric thresholds ranges can be extended for a larger sample on the sensitivity test, or even the water vapor mixing ratio threshold can be perturbed to see its effect on the identification. Although the high false alarm ratio of automatically detected drylines is still difficult to reduce with our current identification approach (Clark et al. 2015), it is hypothesized that even an increase of the humidity gradient threshold value to, for instance 0.06 g/kg/km could significantly reduce FAR.A promising way forward is to create a catalogue of manually detected drylines by an experienced forecaster, such as the one used in Coffer et al. (2013), to train a machine learning algorithm and improve the automatic detection (Clark et al. 2015). Furthermore, limitations in the multi-parametric algorithm to automatically detect drylines might also be considered to improve the detection of drylines. For instance, MacKenzie (2013) highlighted (1) the need to include the vertical dimension to account for the moisture gradient extension above the surface and (2) the idea of intersecting this algorithm with a fronts detection tools to eliminate the possibility of overextension of drylines (e.g. Parsons et al. 2000). In addition, other ideas could focus on improving the use of the smoothing Gaussian filter, which can decrease the number of narrow drylines captured when the algorithm is applied in a numerical model that is only in the meso-gamma scale, or to improve the non-maximum suppression algorithm to include double drylines (e.g. Ziegler et al. 1995; Weiss et al. 2006).

In the future PGW climate, the dryline is projected to significantly increase its frequency and intensity in all subdomains. In the two northern subdomains (CR and NUS), the PGW simulation shows mean monthly dryline magnitudes for September that are comparable to those in June and July from the CTRL simulation. This shows an extension of the dryline environments into the fall, potentially also extending the convective season, and affecting agricultural planning in the Central U.S. Furthermore, in the southern subdomains, morning drylines in the PGW are as strong as historical afternoon drylines, which could increase the likelihood of convective initiation in the morning. Some future changes can be linked to the average increase in the large-scale humidity gradient. For example, the stronger increase of humidity in the eastern U.S. compared to the West (Figure 9a) produces an increase in the humidity gradient along the lee side of the Rocky Mountains (Figure 9b). This change is partly associated to the intensification of the meridional wind transporting moisture from the Gulf of Mexico, east of the Rocky Mountains, whereas the West side of the Rockies shows smaller increases in moisture advection (Fig 9c).

This study does not account for potential changes in future land-cover types, which can affect the surface water mass and energy fluxes as well as soil moisture feedbacks (Johnson and Hitchens 2018, Zhang et al. 2020). Additionally, the PGW approach does not capture systematic changes in the frequency of weather patterns (at the synoptic scale) under future climate conditions. The impact of such changes on drylines in North America should be the focus of future research.

6 Conclusion

We show that the main characteristics of drylines can be diagnosed using a novel automatic algorithm to detect drylines based on climate data from convection-permitting models. These findings are expected to contribute to a better understanding of the dryline in the current climate and how it might change in the future in North America.

Drylines are important because they have been shown to impact CI, and thus indexes that connect both CI and the presence of dryline can help to integrate the analysis in a climatological scale. For example, the solenoidal term (vorticity equation) forces a secondary circulation induced by the dryline, which is a key to increase uplift of air parcels (Ziegler and Rasmussen 1998; Miao and Geerts 2007), or the horizontal shearing stability characterizing the initial stage of vortices development (Buban and Ziegler 2016), or a low minimum buoyancy to initiate convection (Trier et al. 2015). These examples based on case studies could help to develop a more physically meaningful standardization of the dryline definition where/when CI is relevant. This raises interesting questions about the dependence of these processes on the environment, latitude, or other regional characteristic that can define how strong a dryline should be to initiate convection. This question is particularly important in cases where triggering convection might be severe (e.g., Hill et al. 2016).

This study highlights the need for a unified definition of drylines, and our automated algorithm is a step forward towards such definition; however, further testing across different regions is needed. We provide this analysis as an effort to merge concepts in the climate and forecasting research communities, which allows to analyze mesoscale features that are critical in weather forecasting in a climate change context.

Acknowledgments

We gratefully acknowledge the financial support from the *Natural Sciences and Engineering Research Council* of Canada (*NSERC*) Discovery Grant, and the Tri-agency Institutional Programs Secretariat of Canada through the Global Water Futures Program, Canada First Research Excellence Fund. We also acknowledge the support from the Water System Program at the National Center for Atmospheric Research (NCAR). The National Science Foundation sponsors NCAR. This project was performed at the NCAR facilities funded through NSF-Water System Program. We would like to acknowledge high-performance computing support from Yellowstone (ark:/85065/ d7wd3xhc) and Cheyenne (2017, doi: 10.5065/D6RX99HX), provided by NCAR's Computational and Information System Laboratory, sponsored by the National Science Foundation. Era-5 from ECMWF 2017 was stored in the Research Data Archive data DS633.0. AJC contributed to this work as part of regular duties at the federally funded NOAA/National Severe Storms Laboratory.

References

Arnup SJ, Reeder MJ (2007) The Diurnal and Seasonal Variation of the Northern Australian Dryline. Mon Weather Rev 135:2995–3008. https://doi.org/10.1175/MWR3455.1

Bechis H, Salio P, Ruiz JJ (2020) Drylines in Argentina: Synoptic Climatology and Processes Leading to Their Genesis. Mon Weather Rev 148:MWR-D-19-0050.1. https://doi.org/10.1175/MWR-D-19-0050.1

Bergmaier PT, Geerts B (2015) Characteristics and Synoptic Environment of Drylines Occurring over the Higher Terrain of Southeastern Wyoming. Weather Forecast 30:1733–1748. https://doi.org/10.1175/WAF-D-15-0061.1

Buban MS, Ziegler CL (2016) The Formation of Small-Scale Atmospheric Vortices via Horizontal Shearing Instability. J Atmos Sci 73:2061–2084. https://doi.org/10.1175/JAS-D-14-0355.1

Buban MS, Ziegler CL, Rasmussen EN, Richardson Y (2007) The Dryline on 22 May 2002 during IHOP: Ground-Radar and In Situ Data Analyses of the Dryline and Boundary Layer Evolution. Mon Weather Rev 135:2473–2505. https://doi.org/10.1175/MWR3453.1

Campbell PC, Geerts B, Bergmaier PT (2013) A Dryline in Southeast Wyoming. Part I: Multi-scale Analysis Using Observations and Modeling on 22 June 2010. Mon Weather Rev 130917124004000. https://doi.org/10.1175/MWR-D-13-00049.1

Clark AJ, Coniglio MC, Coffer BE, et al (2015a) Sensitivity of 24-h Forecast Dryline Position and Structure to Boundary Layer Parameterizations in Convection-Allowing WRF Model Simulations. Weather Forecast 30:613–638. https://doi.org/10.1175/WAF-D-14-00078.1

Clark AJ, MacKenzie A, McGovern A, et al (2015b) An Automated, Multiparameter Dryline Identification Algorithm. Weather Forecast 30:1781–1794. https://doi.org/10.1175/WAF-D-15-0070.1

Coffer BE, Maudlin LC, Veals PG, Clark AJ (2013) Dryline Position Errors in Experimental Convection-Allowing NSSL-WRF Model Forecasts and the Operational NAM. Weather Forecast 28:746–761. https://doi.org/10.1175/WAF-D-12-00092.1

Coniglio MC, Correia J, Marsh PT, Kong F (2013) Verification of Convection-Allowing WRF Model Forecasts of the Planetary Boundary Layer Using Sounding Observations. Weather Forecast 28:842–862. https://doi.org/10.1175/WAF-D-12-00103.1

Dee DP, Uppala SM, Simmons a. J, et al (2011) The ERA-Interim reanalysis: Configuration and performance of the data assimilation system. Q J R Meteorol Soc 137:553–597. https://doi.org/10.1002/qj.828

Duell RS, Van Den Broeke MS (2016) Climatology, synoptic conditions, and misanalyses of Mississippi River valley drylines. Mon Weather Rev 144:927–943. https://doi.org/10.1175/MWR-D-15-0108.1

ECMWF (2017) ERA5 Reanalysis Monthly Means

Erfani A, Goodson R, Bélair S, et al (2003) Synoptic and mesoscale study of a severe convective outbreak with the nonhydrostatic Global Environmental Multiscale (GEM) model. Meteorol Atmos Phys 82:31–53. https://doi.org/10.1007/s00703-001-0585-8

Flanagan PX, Basara JB, Illston BG, Otkin JA (2017) The Effect of the Dry Line and Convective Initiation on Drought Evolution over Oklahoma during the 2011 Drought. Adv Meteorol 2017:. https://doi.org/10.1155/2017/8430743

Fritsch JM, Carbone RE (2004) Improving quantitative precipitation forecasts in the warm season: A USWRP research and development strategy. Bull Am Meteorol Soc 85:955–965. https://doi.org/10.1175/BAMS-85-7-955

Geerts B, Damiani R, Haimov S (2006) Finescale Vertical Structure of a Cold Front as Revealed by an Airborne Doppler Radar. Mon Weather Rev 134:251–271

Gutmann ED, Rasmussen RM, Liu C, et al (2018) Changes in hurricanes from a 13-Yr convection-permitting pseudo- global warming simulation. J Clim 31:3643–3657. https://doi.org/10.1175/JCLI-D-17-0391.1

Hane CE, Ziegler CL, Bluestein HB (1993) Investigation of the Dryline and Convective Storms Initiated along the Dryline: Field Experiments during COPS–91. Bull Am Meteorol Soc 74:2133–2145. https://doi.org/10.1175/1520-0477(1993)074<2133:iotdac>2.0.co;2

Hersbach, H., and Coauthors (2020): The ERA5 global reanalysis. Q. J. R. Meteorol. Soc., 146, 1999–2049, https://doi.org/10.1002/qj.3803.

Hill AJ, Weiss CC, Ancell BC (2016) Ensemble sensitivity analysis for mesoscale forecasts of dryline convection initiation. Mon Weather Rev 144:4161–4182. https://doi.org/10.1175/MWR-D-15-0338.1

Hill LM (2006) Drylines observed in Alberta during A-GAME. University of Alberta

Hoch J, Markowski P (2005) A climatology of springtime dryline position in the U.S. Great Plains region. J Clim 18:2132–2137. https://doi.org/10.1175/JCLI3392.1

Hong S-Y, Noh Y, Dudhia J (2006) A new vertical diffusion package with an explicit treatment of entrainment processes. Mon Weather Rev 134:2318–2341. https://doi.org/10.1175/MWR3199.1

Iacono MJ, Delamere JS, Mlawer EJ, et al (2008) Radiative forcing by long-lived greenhouse gases: Calculations with the AER radiative transfer models. J Geophys Res Atmos 113:2–9. https://doi.org/10.1029/2008JD009944

Johnson ZF, Hitchens NM (2018) Effects of Soil Moisture on the Longitudinal Dryline Position in the Southern Great Plains. J Hydrometeorol 19:273–287. https://doi.org/10.1175/JHM-D-17-0091.1

Liu C, Ikeda K, Rasmussen R, et al (2017) Continental-scale convection-permitting modeling of the current and future climate of North America. Clim Dyn 1–25. https://doi.org/10.1007/s00382-016-3327-9

MacKenzie A (2013) An automated multi-parameter dryline identification and tracking algorithm. University of Oklahoma

Mathworks C (2014) Image Processing Toolbox ™ User ’ s Guide R 2014 b

Miao Q, Geerts B (2007) Finescale vertical structure and dynamics of some dryline boundaries observed in IHOP. Mon Weather Rev 135:4161–4184. https://doi.org/10.1175/2007MWR1982.1

Niu GY, Yang ZL, Mitchell KE, et al (2011) The community Noah land surface model with multiparameterization options (Noah-MP): 1. Model description and evaluation with local-scale measurements. J Geophys Res Atmos 116:1–19. https://doi.org/10.1029/2010JD015139

Parsons DB, Schapiro MA, Hardesty RM, et al (1990) The Finescale Structure of a West Texas Dryline. Mon. Weather Rev. 119:1242–1258

Parsons DB, Shapiro MA, Miller E (2000) The mesoscale structure of a nocturnal dryline and of a frontal-dryline merger. Mon Weather Rev 128:3824–3838. https://doi.org/10.1175/1520-0493(2001)129<3824:TMSOAN>2.0.CO;2

Peckham SE, Wilhelmson RB, Wicker LJ, Ziegler CL (2004) Numerical simulation of the interaction between the dryline and horizontal convective rolls. Mon Weather Rev 132:1792–1812. https://doi.org/10.1175/1520-0493(2004)132<1792:NSOTIB>2.0.CO;2

Peterson RE (1983) The west Texas dryline: Occurrence and behavior. In: Preprints, 13th Conf. on Severe Local Storms, Tulsa, OK, Amer. Meteor. Soc., J9–J11

Powers JG, Klemp JB, Skamarock WC, et al (2017) The weather research and forecasting model: Overview, system efforts, and future directions. Bull Am Meteorol Soc 98:1717–1737. https://doi.org/10.1175/BAMS-D-15-00308.1

Prein AF, Liu C, Ikeda K, et al (2017a) Simulating North American mesoscale convective systems with a convection-permitting climate model. Clim Dyn. https://doi.org/DOI 10.1007/s00382-017-3993-2

Prein AF, Liu C, Ikeda K, et al (2017b) Increased rainfall volume from future convective storms in the US. Nat Clim Chang 7:880–884. https://doi.org/10.1038/s41558-017-0007-7

Prein AF, Rasmussen RM, Ikeda K, et al (2016) The future intensification of hourly precipitation extremes. Nat Clim Chang 7:1–6. https://doi.org/10.1038/nclimate3168

Rasmussen KL, Prein AF, Rasmussen RM, et al (2017) Changes in the convective population and thermodynamic environments in convection-permitting regional climate simulations over the United States. Clim Dyn 0:1–26. https://doi.org/10.1007/s00382-017-4000-7

Rasmussen R, Liu C, Ikeda K, et al (2011) High-resolution coupled climate runoff simulations of seasonal snowfall over Colorado: A process study of current and warmer climate. J Clim 24:3015–3048. https://doi.org/10.1175/2010JCLI3985.1

Rhea JO (1966) A Study of Thunderstorm Formation Along Dry Lines. J. Appl. Meteorol. 5:58–63

Riahi K, Rao S, Krey V, et al (2011) RCP 8.5-A scenario of comparatively high greenhouse gas emissions. Clim Change 109:33–57. https://doi.org/10.1007/s10584-011-0149-y

Roebber PJ (2009) Visualizing multiple measures of forecast quality. Weather Forecast 24:601–608. https://doi.org/10.1175/2008WAF2222159.1

Saha S, Moorthi S, Pan H, Wu X (2010) The NCEP climate forecast system reanalysis. BAMS 1015–1057. https://doi.org/10.1175/2010Bams3001.1

Scaff L, Prein AF, Li Y, et al (2019) Simulating the convective precipitation diurnal cycle in North America's current and future climate. Clim Dyn. https://doi.org/10.1007/s00382-019-04754-9

Schaefer JT (1974) The Life Cycle of the Dryline. J. Appl. Meteorol. 13:444–449

Schaefer JT (1973) The motion and morphology of the dryline. US Department of Commerce, National Oceanic and Atmospheric Administration, Environmental Research Laboratories, National Severe Storms Laboratory

Schär C, Frei C, Lüthi D, Davies HC (1996) Surrogate climate‐change scenarios for regional climate models. Geophys Res Lett 23:669. https://doi.org/10.1029/96GL00265

Skamarock, W. C., 2004: Evaluating Mesoscale NWP Models Using Kinetic Energy Spectra. Mon. Wea. Rev., 132, 2019-3032.

Skamarock WC, Klemp JB, Dudhia J, et al (2008) A description of the advanced research WRF version 3. NCAR Technical Note NCAR/TN-475 + STR.

Strong GS (1989) LIMEX-85: 1 . Processing of Data Sets from an Alberta Mesoscale U pper-Air Experiment. Climatol Bull 23:98–118

Sun C, Vallotton P (2009) Fast linear feature detection using multiple directional non-maximum suppression. J Microsc 234:147–157. https://doi.org/10.1111/j.1365-2818.2009.03156.x

Sun W-Y, Wu C-C (1992) Formation and Diurnal Variation of the Dryline. J Atmos Sci 49:1606–1620

Taylor KE, Stouffer RJ, Meehl GA (2012) An overview of CMIP5 and the experiment design. Bull Am Meteorol Soc 93:485–498. https://doi.org/10.1175/BAMS-D-11-00094.1

Taylor NM, Sills DML, Hanesiak JM, et al (2011) The understanding severe thunderstorms and Alberta boundary layers experiment (UNSTABLE) 2008

Thompson G, Eidhammer T (2014) A Study of Aerosol Impacts on Clouds and Precipitation Development in a Large Winter Cyclone. J Atmos Sci 71:3636–3658. https://doi.org/10.1175/JAS-D-13-0305.1

Trier SB, Chen F, Manning KW (2004) A Study of Convection Initiation in a Mesoscale Model Using High-Resolution Land Surface Initial Conditions. Mon Weather Rev 132:2954–2976. https://doi.org/10.1175/MWR2839.1

Trier SB, Romine GS, Ahijevych DA, et al (2015) Mesoscale Thermodynamic Influences on Convection Initiation near a Surface Dryline in a Convection-Permitting Ensemble. Mon Weather Rev 143:3726–3753. https://doi.org/10.1175/MWR-D-15-0133.1

Weeks AR (1996) Fundamentals of Electronic Image Processing. Wiley-IEEE Press.

Weiss CC, Bluestein HB, Pazmany AL (2006) Finescale Radar Observations of the 22 May 2002 Dryline during the International H_2O Project (IHOP). Mon Weather Rev 134:273–293. https://doi.org/10.1175/MWR3068.1

Weston KJ (1972) The dry‑line of Northern India and its role in cumulonimbus convection. Q J R Meteorol Soc 98:519–531

Wilks DS (2011) Statistical methods in the atmospheric sciences, Third Edit. Academic press

Wilson JW, Roberts RD (2006) Summary of Convective Storm Initiation and Evolution during IHOP: Observational and Modeling Perspective. Mon Weather Rev 134:23–47. https://doi.org/10.1175/MWR3069.1

Wilson JW, Schreiber WE (1986) Initiation of convective storms at radar-observed boundary layer convergence lines. Mon Weather Rev 114:2516–2536. https://doi.org/10.1175/1520-0493(1986)114<2516:IOCSAR>2.0.CO;2

Xue M, Martin WJ (2006) A High-Resolution Modeling Study of the 24 May 2002 Dryline Case during IHOP. Part II: Horizontal Convective Rolls and Convective Initiation. Mon Weather 134:172–193

Zhang, Z., Y. Li, F. Chen, M. Barlage, and Z. Li, (2020) Evaluation of convection-permitting WRF CONUS simulation on the relationship between soil moisture and heatwaves. Clim. Dyn., 0, 0, https://doi.org/10.1007/s00382-018-4508-5.

Ziegler CL, Martin WJ, Pielke RA, Walko RL (1995) A modeling study of the dryline. J. Atmos. Sci. 52:263–285

Ziegler CL, Lee TJ, Pielke R a. (1997) Convective Initiation at the Dryline: A Modeling Study. Mon Weather Rev 125:1001–1026. https://doi.org/10.1175/1520-0493(1997)125<1001:CIATDA>2.0.CO;2

Ziegler CL, Rasmussen EN (1998) The Initiation of Moist Convection at the Dryline: Forecasting Issues from aCase Study Perspective. Weather Forecast 13:1106–1131. https://doi.org/10.1175/1520-0434(1998)013<1106:TIOMCA>2.0.CO;2

Geerts B, Damiani R, Haimov S (2006) Finescale Vertical Structure of a Cold Front as Revealed by an Airborne Doppler Radar. Mon Weather Rev 134:251–271

Miao Q, Geerts B (2007) Finescale vertical structure and dynamics of some dryline boundaries observed in IHOP. Mon Weather Rev 135:4161–4184. https://doi.org/10.1175/2007MWR1982.1

Parsons DB, Shapiro MA, Miller E (2000) The mesoscale structure of a nocturnal dryline and of a frontal-dryline merger. Mon Weather Rev 128:3824–3838. https://doi.org/10.1175/1520-0493(2001)129<3824:TMSOAN>2.0.CO;2

Peckham SE, Wilhelmson RB, Wicker LJ, Ziegler CL (2004) Numerical simulation of the interaction between the dryline and horizontal convective rolls. Mon Weather Rev 132:1792–1812. https://doi.org/10.1175/1520-0493(2004)132<1792:NSOTIB>2.0.CO;2

Sipprell BD, Geerts B (2007) Finescale vertical structure and evolution of a preconvective dryline on 19 June 2002. Mon Weather Rev 135:2111–2134. https://doi.org/10.1175/MWR3354.1

Weiss CC, Bluestein HB, Pazmany AL (2006) Finescale Radar Observations of the 22 May 2002 Dryline during the International H_2O Project (IHOP). Mon Weather Rev 134:273–293. https://doi.org/10.1175/MWR3068.1

Weston KJ (1972) The dry‑line of Northern India and its role in cumulonimbus convection. Q J R Meteorol Soc 98:519–531

Xue M, Martin WJ (2006) A High-Resolution Modeling Study of the 24 May 2002 Dryline Case during IHOP. Part I: Numerical Simulation and General Evolution of the Dryline and Convection. Mon Weather Rev 134:149–171

Ziegler CL, Lee TJ, Pielke R a. (1997) Convective Initiation at the Dryline: A Modeling Study. Mon Weather Rev 125:1001–1026. https://doi.org/10.1175/1520-0493(1997)125<1001:CIATDA>2.0.CO;2

Ziegler CL, Martin WJ, Pielke RA, Walko RL (1995) A modeling study of the dryline. J. Atmos. Sci. 52:263–285

Ziegler CL, Rasmussen EN (1998) The initiation of moist convection at the dryline: Forecasting issues from a case study perspective. Weather Forecast 13:1106–1131. https://doi.org/10.1175/1520-0434(1998)013<1106:TIOMCA>2.0.CO;2

Table 1 Model description of the CTRL and the PGW. $CTRL_{BC}$ is the boundary conditions for the control simulation. GCM means Global Climate Models, CMIP5 means Coupled Models Intercomparison Project Phase 5. RCP8.5 means the Representative Concentration Pathway with 8.5 W/m^2

WRF version	Advanced Research WRF V3.4.1.
Domain extent	Appox.19-57°N, 139-56°W From approx. 140 m below the ground to up to 50 hPa (~ 20,000 m a.s.l.)
Resolution	spatial: 4 km, temporal: 1 hour
Boundary conditions (BC)	$CTRL_{BC}$: ERA-Interim Reanalysis every 6 hours PGW: $CTRL_{BC}$ + ΔCMIP5 (of 20 GCM w/RCP8.5, in 2070-2099)
Initial and boundary input variables	Soil and air temperature, geopotential height, wind speed, soil moisture, atmospheric pressure, and specific humidity.
Spin up period	3 months
Main physical Schemes	
>Microphysics	New Thompson and Eidhammer (2014)
>Land-surface	Noah Multi-Physics (Noah-MP Niu et al 2011)
>Planetary boundary layer	Yonsei University (YSU, Hong et al 2006)
>Cumulus	No cumulus parameterization used.
>Long- and short-wave	Radiative Transfer model (RRTMG, Iacono et al 2008)

Table 2 131 Documented dates with drylines from Geerts et al. 2006, Coffer et al. 2013 and Clark et al. 2015 that are present in the CTRL simulation.

Documented dryline dates (dd/mmm/yyyy hh)				
11/Apr/2007 00	13/May/2008 00	16/Jun/2009 00	20/Apr/2011 00	02/Apr/2012 00
20/Apr/2007 00	23/May/2008 00	05/Apr/2010 00	22/Apr/2011 00	03/Apr/2012 00
21/Apr/2007 00	24/May/2008 00	06/Apr/2010 00	23/Apr/2011 00	07/Apr/2012 00
22/Apr/2007 00	27/May/2008 00	07/Apr/2010 00	25/Apr/2011 00	12/Apr/2012 00
23/Apr/2007 00	01/Jun/2008 00	30/Apr/2010 00	26/Apr/2011 00	13/Apr/2012 00
24/Apr/2007 00	04/Jun/2008 00	07/May/2010 00	27/Apr/2011 00	14/Apr/2012 00
25/Apr/2007 00	05/Jun/2008 00	10/May/2010 00	09/May/2011 00	15/Apr/2012 00
05/May/2007 00	06/Jun/2008 00	11/May/2010 00	10/May/2011 00	28/Apr/2012 00
06/May/2007 00	07/Jun/2008 00	12/May/2010 00	12/May/2011 00	29/Apr/2012 00
07/May/2007 00	08/Jun/2008 00	13/May/2010 00	13/May/2011 00	30/Apr/2012 00
23/May/2007 00	11/Jun/2008 00	20/May/2010 00	18/May/2011 00	02/May/2012 00
24/May/2007 00	12/Jun/2008 00	22/May/2010 00	19/May/2011 00	03/May/2012 00
30/May/2007 00	05/Apr/2009 00	23/May/2010 00	20/May/2011 00	04/May/2012 00
02/Jun/2007 00	10/Apr/2009 00	24/May/2010 00	21/May/2011 00	19/May/2012 00
07/Jun/2007 00	18/Apr/2009 00	25/May/2010 00	22/May/2011 00	20/May/2012 00
08/Jun/2007 00	19/Apr/2009 00	12/Jun/2010 00	24/May/2011 00	24/May/2012 00
01/Apr/2008 00	27/Apr/2009 00	13/Jun/2010 00	25/May/2011 00	25/May/2012 00
04/Apr/2008 00	30/Apr/2009 00	14/Jun/2010 00	28/May/2011 00	26/May/2012 00
08/Apr/2008 00	01/May/2009 00	18/Jun/2010 00	29/May/2011 00	28/May/2012 00
10/Apr/2008 00	02/May/2009 00	04/Apr/2011 00	30/May/2011 00	31/May/2012 00
17/Apr/2008 00	06/May/2009 00	08/Apr/2011 00	31/May/2011 00	10/Jun/2012 00
21/Apr/2008 00	09/May/2009 00	09/Apr/2011 00	12/Jun/2011 00	11/Jun/2012 00
22/Apr/2008 00	14/May/2009 00	10/Apr/2011 00	17/Jun/2011 00	19/Jun/2012 00
24/Apr/2008 00	10/Jun/2009 00	14/Apr/2011 00	18/Jun/2011 00	20/Jun/2012 00
25/Apr/2008 00	12/Jun/2009 00	15/Apr/2011 00	21/Jun/2011 00	21/Jun/2012 00
01/May/2008 00	13/Jun/2009 00	19/Apr/2011 00	26/Jun/2011 00	27/Jun/2012 00
02/May/2008 00				

Table 3 19 parameters combination to evaluate the automatic algorithm sensitivity against the 131 drylines documented and presented in Table 2. The bold font shows the parameter combination that is selected for this study.

Sensitivity analysis, parameters combination			
	Bounding box		**Vapor pressure gradient (Pa km^{-1})**
Experiment	**Width (km)**	**Length (km)**	
1	180	400	0
2	180	400	6.25
3	180	400	9.375
4	220	400	0
5	180	500	0
6	220	500	0
7	180	600	0
8	**220**	**600**	**0**
9	100	800	0
10	140	800	0
11	100	180	6.25
12	100	180	9.375
13	100	180	12.5
14	140	180	6.25
15	140	180	9.375
16	140	180	12.5
17	180	180	6.25
18	180	180	9.375
19	180	180	12.5

Table 4 Subdomain summary of the dryline frequency, the average magnitude, and the mean major axis length.

	Number of hours with dryline at 00 UTC Apr-Sep			**Average magnitude ($g\ kg^{-1}\ km^{-1}$)**			**Average major axis length (km)**		
domain	**CTRL**	**PGW**	**Difference**	**CTRL**	**PGW**	**Difference**	**CTRL**	**PGW**	**Difference**
CR	9%	16%	7%	0.129	0.144	11%	555.8	551.7	-1%
NUS	25%	30%	5%	0.147	0.163	10.6%	428.9	423.5	-1%
SUS	47%	51%	4%	0.177	0.203	15%	636.3	626.9	-1%
NMX	26%	29%	3%	0.194	0.223	15%	349.8	367.2	5%
AVG	**27%**	**31%**	**5%**	**0.162**	**0.183**	**13%**	**493**	**492**	**0%**

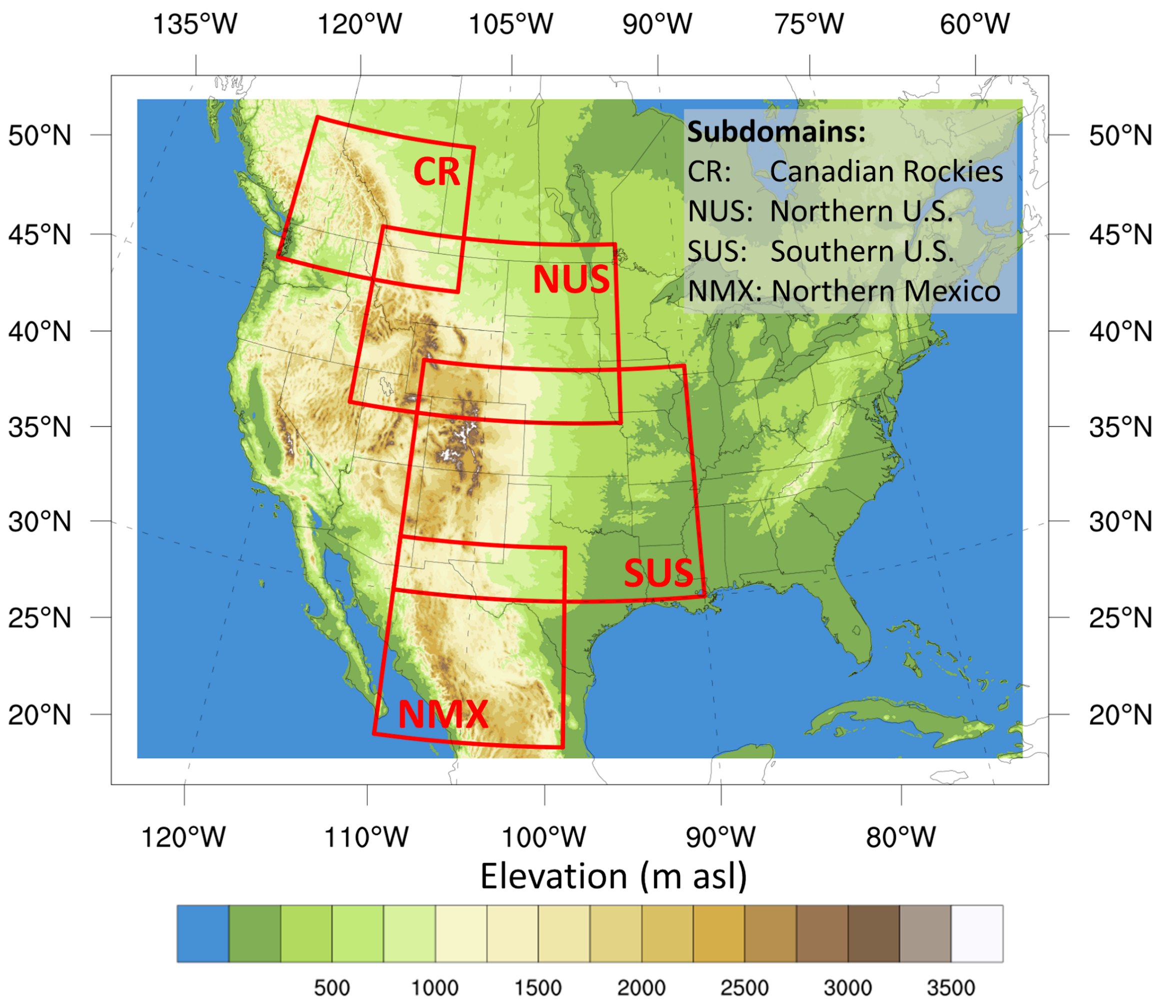

Figure 1 Simulated domain with topography in colors. The four subdomains are highlighted in red squares, which overlap 3° in latitude.

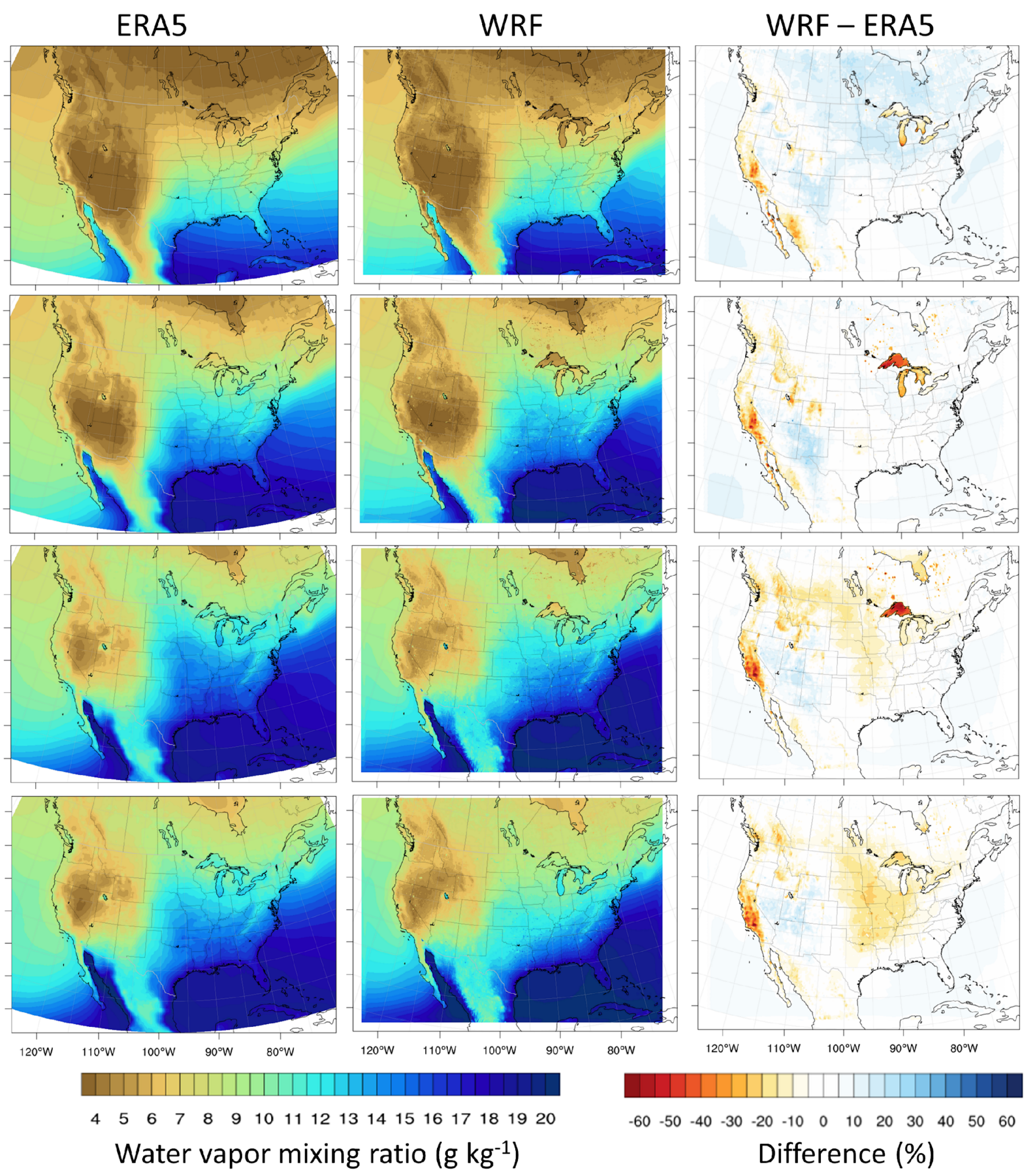

Figure 2 Water vapor mixing ratio of 13-years monthly average. Left column shows ERA5 reanalysis, the central column shows WRF CTRL simulation, and the right column shows the difference in percentage.

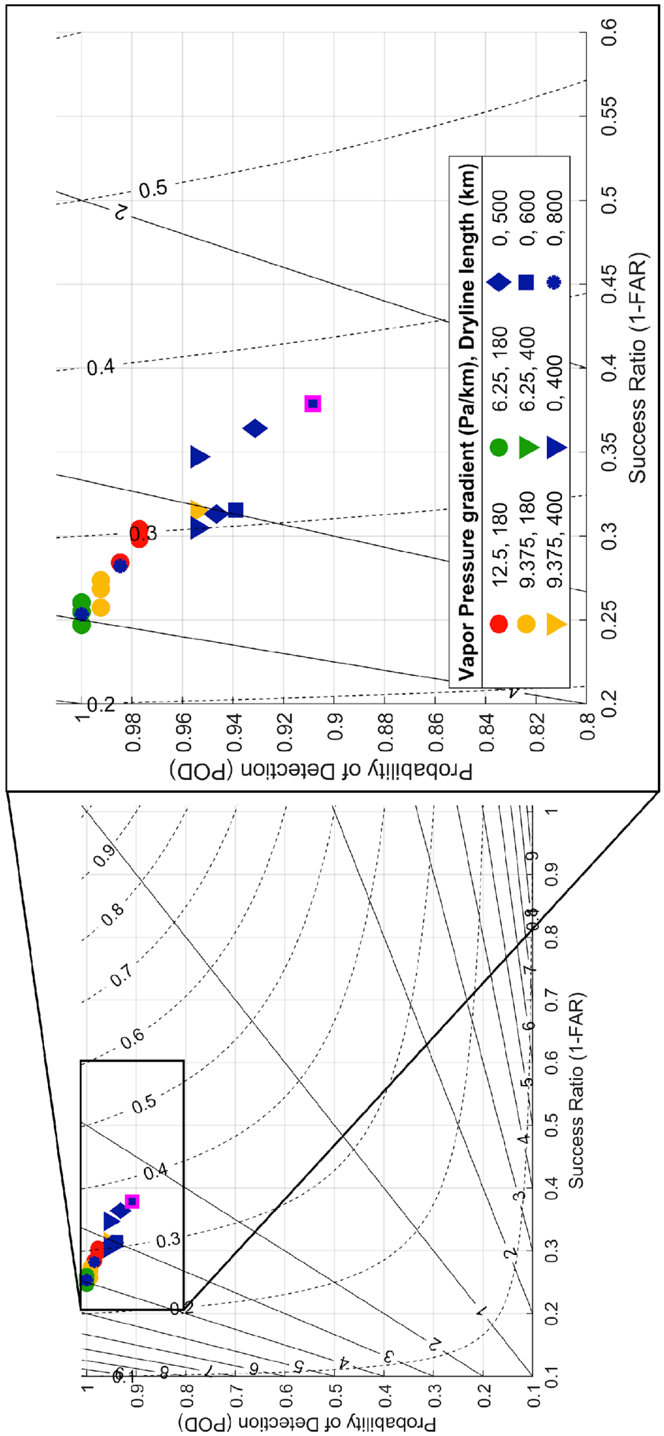

Figure 3 Performance diagram (Roebber 2009) showing the sensitivity tests over the southern US. Diagonal solid lines show bias scores and thinner dashed lines shows the Critical Success Index (CSI). Legend displays experiments with different thresholds of minimum vapor pressure gradient (in Pa/km) and minimum dryline length (km). The detection rate is calculated over the total number of cases, 131 events in SUS. The magenta square in the plot is highlighting the selected combination of parameters to perform the dryline detection.

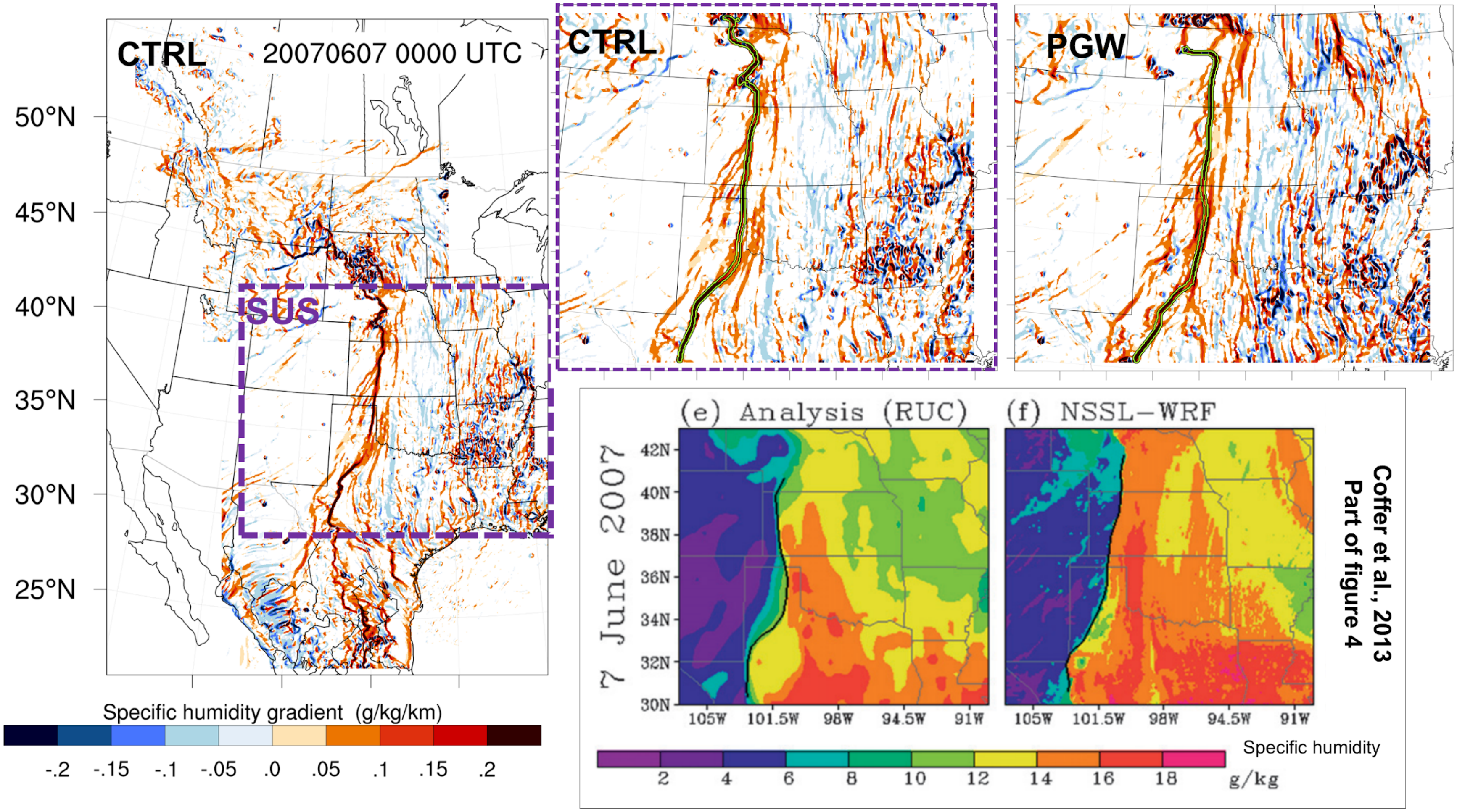

Figure 4 Example of an automatic dryline detection in 07 June 2007, at 00 UTC. The left panel shows the entire domain with drylines along the east of the Rocky Mountains for CTRL simulation. Zoom in to the southern U. S. subdomain (upper right panel) is presented with green contour enclosing the area of automatic dryline identification for the CTRL and the PGW simulations. The lower right panel shows the manual identification of the dryline in the southern U.S. in the same date from Coffer et al., 2013.

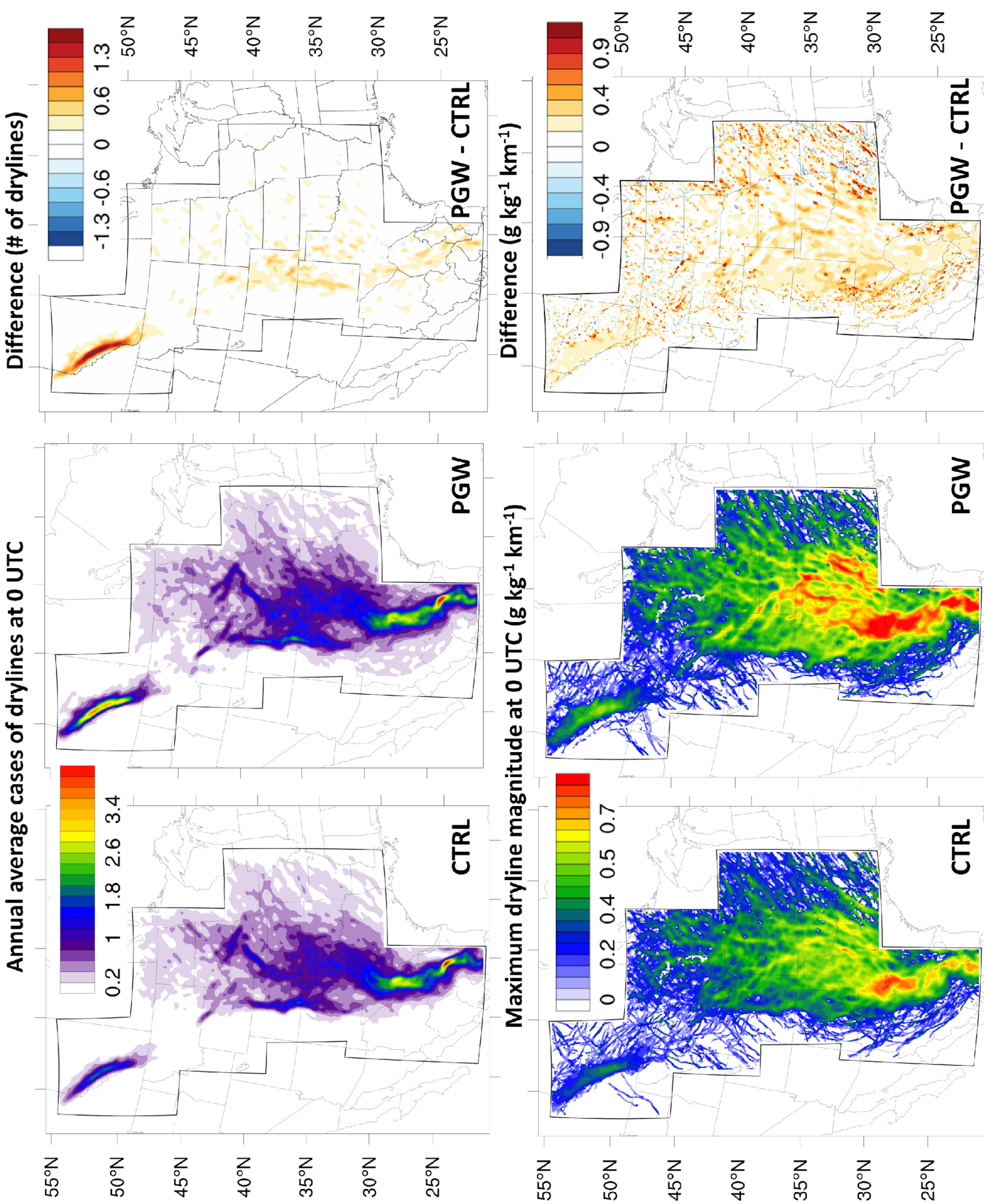

Figure 5 Average frequency and maximum magnitude of drylines for the 13-year simulations between April and September at 00 UTC (upper and lower panels respectively). The left panel shows the CTRL simulation, the middle panel the PGW simulation, and the right panel the

difference between them.

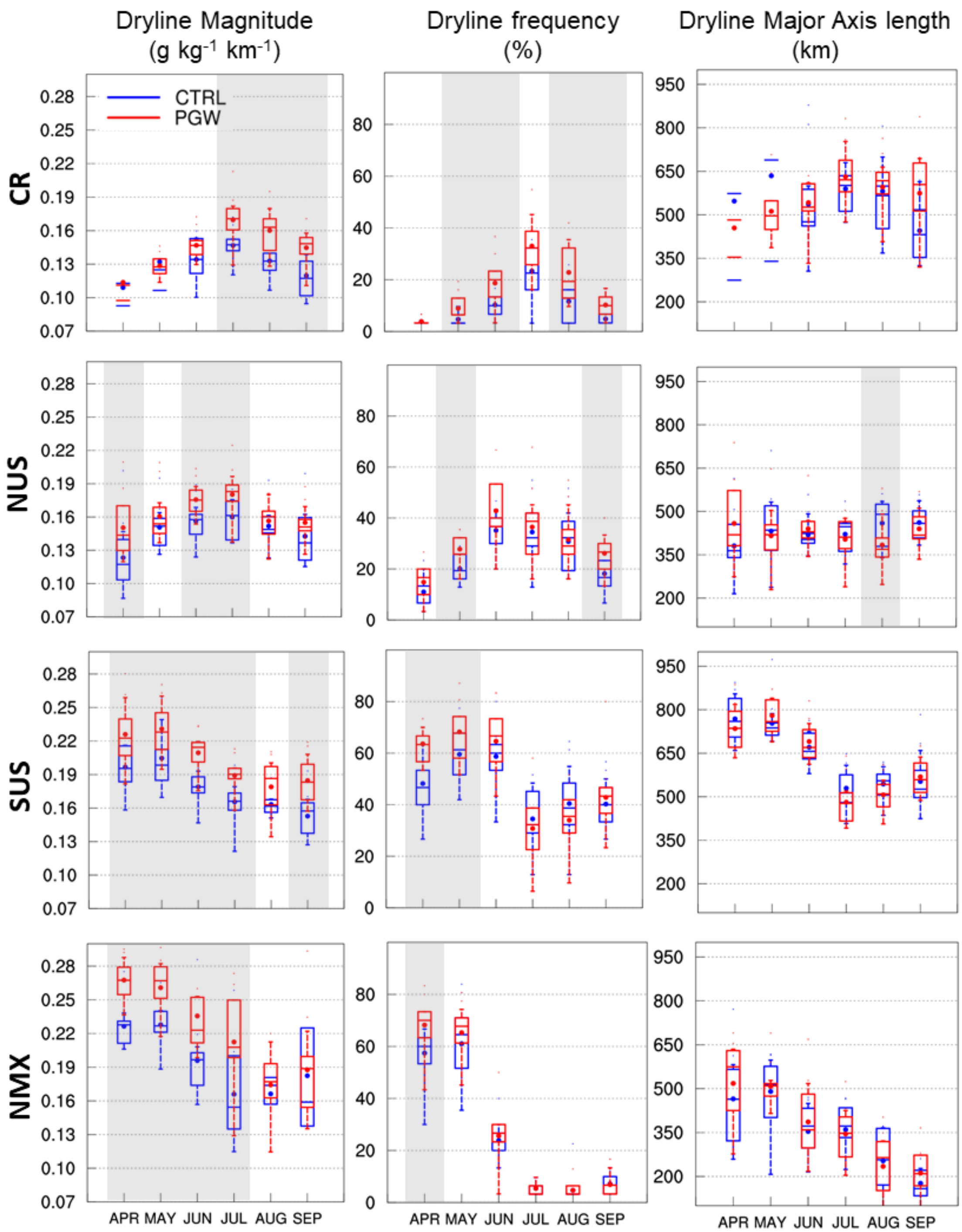

Figure 6 Seasonal variation at 00 UTC of the dryline magnitude (left column), frequency (center column) and major axis length (right column), over the Canadian Rockies (CR), the northern and southern U.S. (NUS, SUS) and northern Mexico (NMX). Grey areas show months with a statistically significant change between PGW (red) and CTRL (blue) simulations. The dryline frequency is larger compared with the number of drylines per pixel in Figure 5, this difference is due to the approach used to explain spatial changes per each grid cell, rather than calculating the

integrate temporal changes in the entire subdomain.

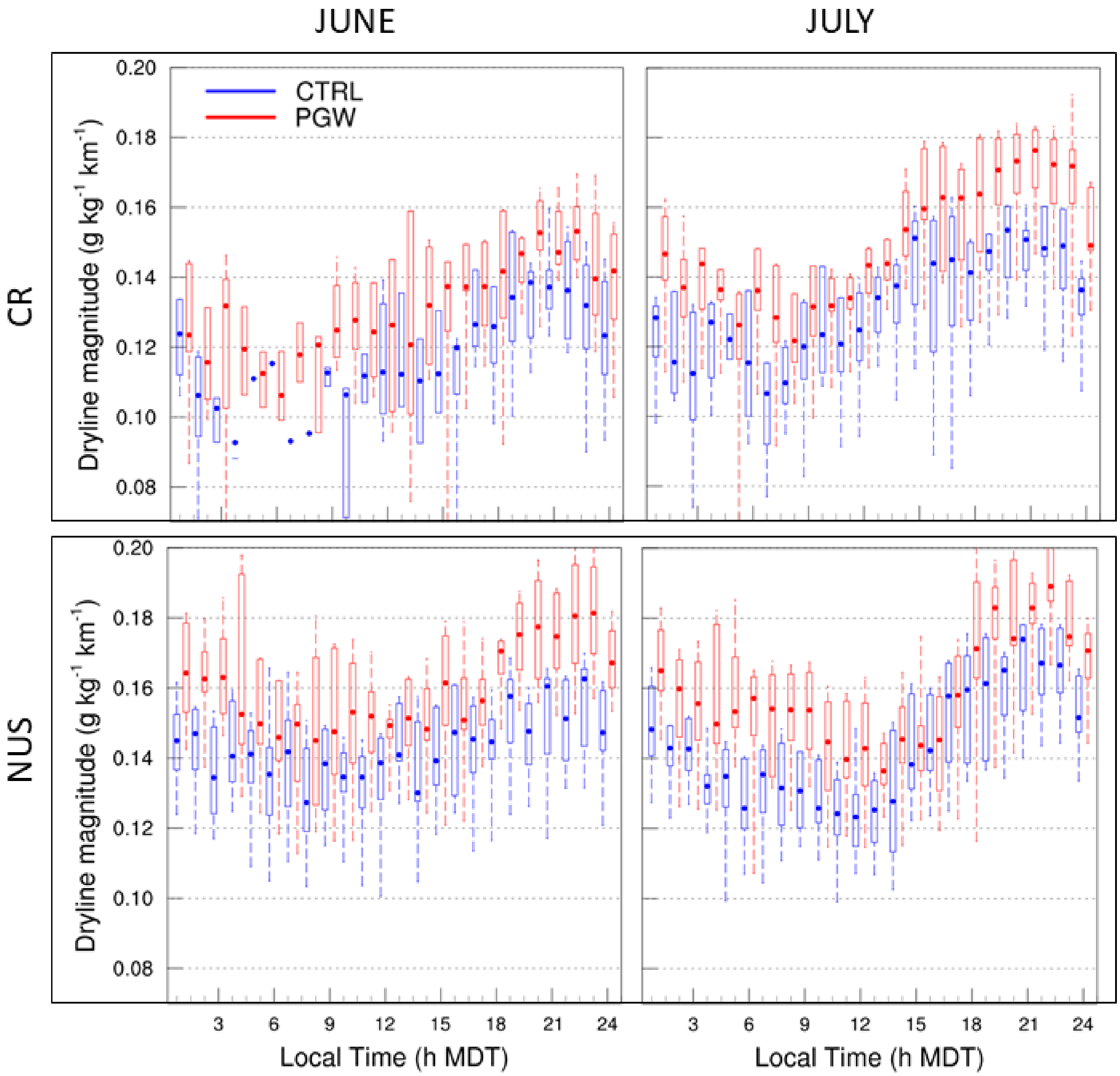

Figure 7 Diurnal cycle of the dryline magnitude in the Canadian Rockies (CR) and the northern U.S.(NUS) in June and July. Blue boxplots represent the CTRL simulation and red ones represent the PGW. The local time is presented in Mountain Daylight time (MDT).

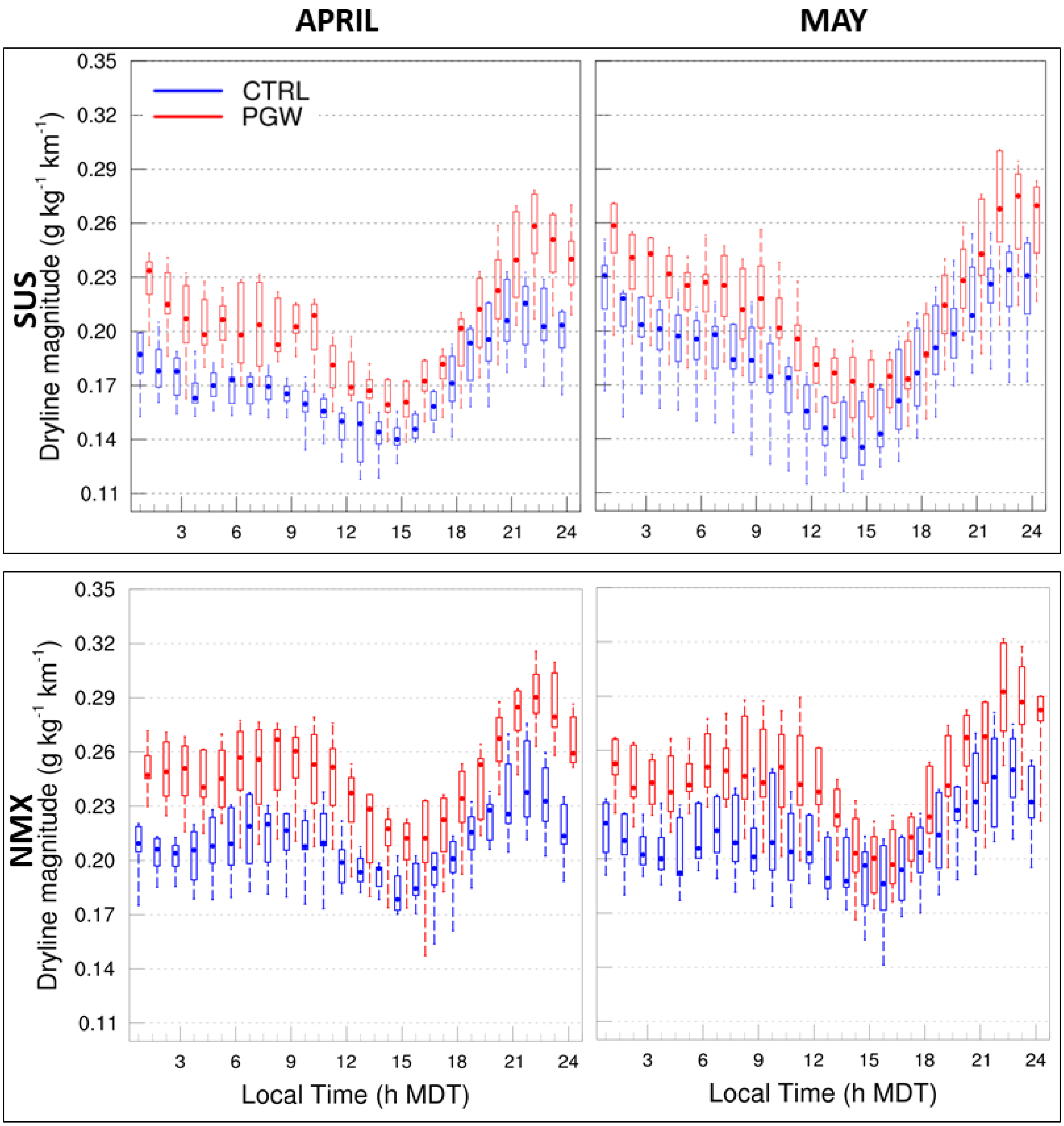

Figure 8 Diurnal cycle of the dryline magnitude in the southern U.S. (SUS) and northern Mexico (NMX) in April and May. Blue boxplots represent the CTRL simulation and red ones represent the PGW. The local time is presented in Mountain Daylight time (MDT).

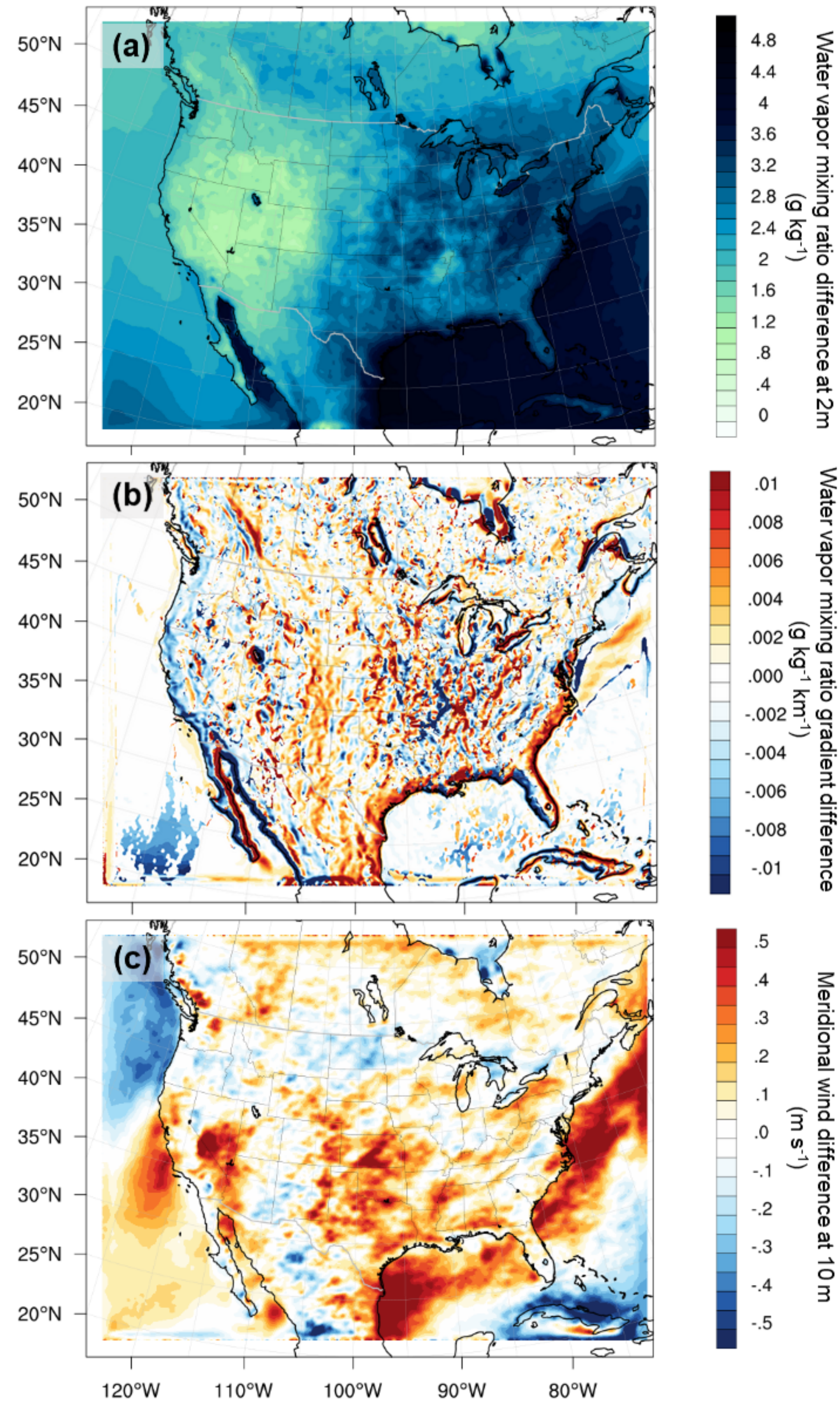

(a)
(b)
(c)
50°N
45°N
40°N
35°N
30°N
25°N
20°N
120°W
110°W
100°W
90°W
80°W
Water vapor mixing ratio difference at 2m (g kg-1)
4.8
4.4
4
3.6
3.2
2.8
2.4
2
1.6
1.2
.8
.4
0
Water vapor mixing ratio gradient difference (g kg-1 km-1)
.01
.008
.006
.004
.002
.000
-.002
-.004
-.006
-.008
-.01
Meridional wind difference at 10 m (m s-1)
.5
.4
.3
.2
.1
.0
-.1
-.2
-.3
-.4
-.5

Figure 9 Difference between PGW and CTRL maps in June at 00 UTC, for: water vapor mixing ratio at 2 m (a) its spatial gradient (b), and the meridional wind at 10 m (c).